An efficient threshold dynamics method for wetting on rough surfaces

Xianmin Xu[a], Dong Wang[b], Xiao-Ping Wang[b,*]

[a] *LSEC, Institute of Computational Mathematics and Scientific/Engineering Computing, NCMIS, AMSS, Chinese Academy of Sciences, Beijing 100190, China*
[b] *Department of Mathematics, The Hong Kong University of Science and Technology, Hong Kong*

arXiv:1602.04688v2 [math.NA] 16 Oct 2016

Abstract

The threshold dynamics method developed by Merriman, Bence and Osher (MBO) is an efficient method for simulating the motion by mean curvature flow when the interface is away from the solid boundary. Direct generalization of MBO-type methods to the wetting problem with interfaces intersecting the solid boundary is not easy because solving the heat equation in a general domain with a wetting boundary condition is not as efficient as it is with the original MBO method. The dynamics of the contact point also follows a different law compared with the dynamics of the interface away from the boundary. In this paper, we develop an efficient volume preserving threshold dynamics method for simulating wetting on rough surfaces. This method is based on minimization of the weighted surface area functional over an extended domain that includes the solid phase. The method is simple, stable with $O(N \log N)$ complexity per time step and is not sensitive to the inhomogeneity or roughness of the solid boundary.

Keywords: Threshold dynamics method, wetting, rough surface

1. Introduction

Wetting describes how a liquid drop spreads on a solid surface. The most important quantity in wetting is the contact angle between the liquid surface and the solid surface [8]. When the solid surface is homogeneous, the contact angle for a static drop is given by the famous Young's equation:

$$\cos\theta_Y = \frac{\gamma_{SV} - \gamma_{SL}}{\gamma_{LV}}, \tag{1}$$

where γ_{SL}, γ_{SV} and γ_{LV} are the solid-liquid, solid-vapor and liquid-vapor surface energy densities, respectively. θ_Y is the so-called Young's angle [35]. Mathematically, Young's equation (1) can be derived by

*Corresponding author
Email addresses: xmxu@lsec.cc.ac.cn (Xianmin Xu), dwangaf@connect.ust.hk (Dong Wang), mawang@ust.hk (Xiao-Ping Wang)

minimizing the total energy in the solid-liquid-vapor system. If we ignore gravity, the total energy in the system can be written as

$$\mathcal{E} = \gamma_{LV}|\Sigma_{LV}| + \gamma_{SL}|\Sigma_{SL}| + \gamma_{SV}|\Sigma_{SV}|, \tag{2}$$

where Σ_{LV}, Σ_{SL} and Σ_{SV} are respectively the liquid-vapor, solid-liquid and solid-vapor interfaces, and $|\cdot|$ denotes the area of the interfaces. When the solid surface Γ is a homogeneous planar surface, under the condition that the volume of the drop is fixed, the unique minimizer of the total energy is a domain with a spherical surface in Ω, and the contact angle between the surface and the solid surface Γ is Young's angle θ_Y[31].

The study of wetting and contact angle hysteresis on rough surfaces is of critical importance for many applications and has attracted much interest in the physics and applied mathematics communities [2, 11, 15, 25, 34]. Numerical simulation of wetting on rough surfaces is challenging. One must track the interface motion accurately, as well as deal with complicated boundary shapes and boundary conditions. There are many different types of numerical methods for solving interface and contact line problems, including the front-tracking method [21, 32], the front-capturing method using the level-set function [36], the phase-field methods [4, 10], among others [9].

Merriman, Bence and Osher (MBO) developed an efficient threshold dynamics method to simulate the motion by mean curvature flow [22, 23]. This method is based on the observation that the level-set of the solution of a heat equation moves in normal direction at a velocity equal to the mean curvature of the level-set surface. The method alternately diffuses and sharpens characteristic functions of regions and is easy to implement and highly efficient. The method was also extended to problems with volume preservation [18, 28] and to some high-order geometric flow problems [13]. Recently, Esedoglu and Otto extended the threshold dynamics method to the multi-phase problems with arbitrary surface tension [12]. There have been many studies on the MBO threshold dynamics method, including some efficient implementations [26, 27, 30] and convergence analysis [3, 5, 14, 17]. In particular, Laux and collaborators established the convergence of some computational algorithms including one with volume preservation[19, 20].

The generalization of MBO-type methods to the wetting problem where interfaces intersecting the boundary is not straightforward because of a lack of integral representation with a heat kernel for a general domain. In the original MBO scheme, when the interface does not intersect the solid boundary, one can solve the heat equation efficiently on a rectangular domain with a uniform grid using convolution of the heat kernel with the initial condition [26, 27]. The convolution can be evaluated using fast Fourier transform (FFT) at $N \log N$ cost per time step where N is the total number of grid points. One way to generalize MBO-type methods to wetting on solid surfaces is to solve the heat equation with a wetting boundary condition before the volume-preserving thresholding step. However, the usual fast algorithms cannot be applied for this case, especially when the boundary is rough.

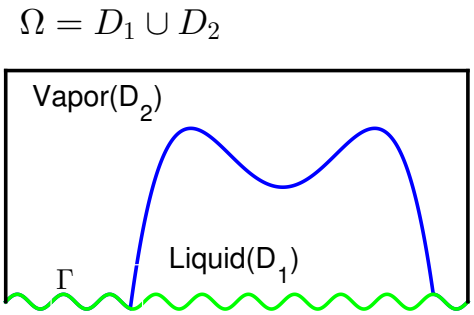

Figure 1: Wetting on a rough surface

In this paper, we aim to develop an efficient volume-preserving threshold dynamics method for solving wetting problems on rough surfaces. Our method is based on the approach of Esedoglu-Otto [12]. The key idea is to extend the original domain with a rough boundary to a regular cube and treat the solid part as another phase. In the thresholding step, the solid phase domain remains unchanged. We show that the algorithm has the total interface energy decaying property and our numerical results show that the equilibrium interface satisfies Young's equation near the contact point. The advantage of the method is that it can be implemented efficiently on uniform meshes with a fast algorithm (e.g. FFT) since the computational domain is rectangular and we can simulate wetting on rough boundaries of any shape. We also introduce a fast algorithm for volume preservation based on a quick-sort algorithm and a time refinement scheme to improve the accuracy of the solution at the contact line.

The paper proceeds as follows. In Section 2, we introduce the surface energies of the wetting problem. A direct (but less efficient) MBO-type threshold dynamics method for solving wetting problems is also described. In Section 3, we introduce a new threshold dynamics method which is simple, efficient and easy to implement. Several modifications of the method are also discussed. In Section 4, we discuss the implementation of the algorithm and perform the accuracy check. We also introduce a quick-sort algorithm for volume preservation and a time refinement technique to improve the accuracy of the contact point motion. In Section 5 and Section 6, we present numerical examples of wetting on rough surfaces to demonstrate the efficiency of the new method.

2. The minimization of surface energies

We consider a wetting problem in a domain $\Omega \in \mathbb{R}^n$, $n = 2, 3$ (see Figure 1). The solid surface Γ is part of the domain boundary $\partial\Omega$. Denote the liquid domain by $D_1 \subset \Omega$. For simplicity, we assume that

$\partial D_1 \cap \partial\Omega \subset \Gamma$. The volume of the liquid drop is fixed such that $|D_1| = V_0$. We denote $\Sigma_{LV} = \partial D_1 \cap \Omega$, $\Sigma_{SL} = \partial D_1 \cap \Gamma$ and $\Sigma_{SV} = \Gamma \setminus \partial D_1$ as the liquid-vapor, solid-liquid and solid-vapor interfaces respectively. Then, the equilibrium configuration of the system is obtained by minimizing the total interface energy of the system as follows:

$$\min_{|D_1|=V_0} \mathcal{E}(D_1) = \gamma_{LV}|\partial D_1 \cap \Omega| + \int_{\partial D_1 \cap \Gamma} \gamma_{SL}(x)\mathrm{d}s + \int_{\Gamma \setminus \partial D_1} \gamma_{SV}(x)\mathrm{d}s \tag{3}$$

where the solid boundary Γ is rough and/or chemically inhomogeneous (i.e. $\gamma_{SL}(x)$ and $\gamma_{SV}(x)$ may depend on x). To ensure the problem is well-posed, Young's angle must satisfy $0 < \theta_Y < \pi$. By equation (1), this leads to the condition $-1 < \frac{\gamma_{SV}-\gamma_{SL}}{\gamma_{LV}} < 1$. Throughout the paper, we will assume this condition holds.

To solve problem (3) numerically, it is convenient to use a diffuse interface model to approximate the sharp interface energy. Suppose φ is a phase-field function, such that $D_1 = \{\varphi < 0\}$ represents the liquid domain, $\{\varphi > 0\}$ represents the vapor domain and $\Sigma_{LV} = \{\varphi = 0\}$ is the liquid-vapor interface. The total energy (2) can be approximated by

$$\mathcal{E}_\varepsilon^{ph}(\varphi) = \int_\Omega \varepsilon|\nabla\varphi|^2 + \frac{f(\varphi)}{\varepsilon}\mathrm{d}\mathbf{x} + \int_\Gamma \gamma(x,\varphi)\mathrm{d}s, \tag{4}$$

where ε is a small parameter representing interface thickness, $f(\varphi) = \frac{(1-\varphi^2)^2}{4}$ is a double-well function and

$$\gamma(\varphi) = \frac{\tilde{\gamma}_{SV}(x) + \tilde{\gamma}_{SL}(x)}{2} + \frac{\tilde{\gamma}_{SV}(x) - \tilde{\gamma}_{SL}(x)}{4}(3\varphi - \varphi^3).$$

It can be proved that when ε goes to zero, after scaling, the energy in (4) converges to that in (2) [33]. Therefore, problem (3) can be approximated by minimizing the total energy $\mathcal{E}_\varepsilon^{ph}$ under the volume constraint $\int_\Omega (\varphi - 1)/2\mathrm{d}\mathbf{x} = V_0$.

The H^{-1} gradient flow of the energy functional (4) will lead to a Cahn-Hilliard equation with contact angle boundary conditions [7]. Alternatively, the L^2 gradient flow will lead to a modified Allen-Cahn equation:

$$\begin{cases} \varphi_t = \varepsilon\Delta\varphi - \frac{f'(\varphi)}{\varepsilon} + \delta & \text{in } \Omega; \\ \frac{\partial\varphi}{\partial n} + \gamma'(x,\varphi) = 0, & \text{on } \Gamma; \\ \frac{\partial\varphi}{\partial n} = 0, & \text{on } \partial\Omega \setminus \Gamma, \\ \int_\Omega \frac{\varphi-1}{2}\mathrm{d}\mathbf{x} = V_0. \end{cases} \tag{5}$$

Here δ is a Lagrangian multiplier for the volume constraint.

A MBO-type threshold dynamics scheme can be derived easily using a splitting method for (5). Assume we have a solution φ^k (characteristic function of a region) at the k-th time step. We can first solve the heat

equation

$$\begin{cases} \bar{\varphi}_t = \varepsilon \Delta \bar{\varphi} & \text{in } \Omega. \\ \frac{\partial \bar{\varphi}}{\partial n} + \gamma'(x, \bar{\varphi}) = 0, & \text{on } \Gamma, \\ \frac{\partial \bar{\varphi}}{\partial n} = 0, & \text{on } \partial\Omega \setminus \Gamma, \\ \bar{\varphi}(x, 0) = \bar{\varphi}^k, \end{cases} \tag{6}$$

for some time δt_1 and then solve

$$\begin{cases} \varphi_t = -\frac{f'(\varphi)}{\varepsilon} \\ \varphi(x, 0) = \bar{\varphi}(x, \delta t_1) \end{cases} \tag{7}$$

for some time δt_2 and set $\varphi^{k+1} = \varphi(x, \delta t_2)$. It is easy to see that when $\delta t_2/\varepsilon$ is large enough, solving the second equation (7) is reduced to a thresholding step

$$\varphi(x, \delta t_2) \approx \begin{cases} -1 & \text{if } \varphi(x, 0) < 0; \\ 1 & \text{if } \varphi(x, 0) > 0, \end{cases} \tag{8}$$

which gives a characteristic function φ^{k+1} at the $k+1$ time step. This leads to the following MBO-type scheme for the wetting problem:

A direct MBO threshold dynamics scheme for the wetting problem

Step 0. *Given an initial domain $D_1^0 \subset \Omega$ such that $|D_1^0| = V_0$. Set a tolerance parameter $\varepsilon > 0$.*

Step 1. *For any k, we first solve the heat equation*

$$\begin{cases} \varphi_t = \Delta \varphi & \text{in } \Omega, \\ \frac{\partial \phi}{\partial n} + \gamma'(x, \varphi) = 0, & \text{on } \Gamma, \\ \frac{\partial \varphi}{\partial n} = 0, & \text{on } \partial\Omega \setminus \Gamma, \\ \varphi(x, 0) = \chi_{D_1^k}, \end{cases} \tag{9}$$

for a time step δt.

Step 2. *Determine a new D_1^{k+1} using thresholding*

$$D_1^{n+1} = \{x : \varphi(x, \delta t) < \frac{1}{2} + \delta\}.$$

Here δ is chosen such that the volume $|D_1^{k+1}| = V_0$.

Step 3. *If $|D_1^k - D_1^{k+1}| < \varepsilon$, stop; otherwise, set $k = k+1$ and go back to Step 1.*

In the original MBO scheme, when the interface does not intersect the solid boundary, one can solve the heat equation efficiently on a uniform grid using convolution of the heat kernel with the initial condition [26, 27]. The convolution can be evaluated using FFT at $M\log(M)$ cost per time step where M is the total number of grid points. However, when the interface intersects the solid boundary, one must solve the heat equation with the wetting boundary condition as in (9). In this case, and in particular for rough boundaries, the usual fast algorithms cannot be applied to solve (9). In the next section, we will introduce a new threshold dynamics method.

3. A new threshold dynamics method for the wetting problem

In this section, we introduce a new threshold dynamics method motivated by the recent work of Esedoglu and Otto [12]. The main idea is to extend the fluid domain Ω to a larger domain containing the solid phase. In the extended domain, the interface energies between different phases in (3) can be approximated by a convolution of characteristic functions and a Guassian kernel (see details below). We then derive a simple scheme to minimize the new energy functional with the constraint that the solid phase does not change and the volume of the liquid phase is preserved. The scheme leads to a new threshold dynamics method for solving the wetting problem.

3.1. The representation of interface energies in an extended domain

In the following, we let $D_1, D_2 \subset \Omega$ be the liquid and vapor phases, respectively. Let $\Sigma_{LV} = \partial D_1 \cap \partial D_2$ be the liquid-vapor interface. When $\delta t \ll 1$, the area of Σ_{LV} can be approximated by (see [1, 24])

$$|\Sigma_{LV}| \approx \frac{1}{\sqrt{\delta t}} \int \chi_{D_1} G_{\delta t} * \chi_{D_2} \mathrm{d}\mathbf{x}, \tag{10}$$

where χ_{D_i} is the characteristic function of D_i and

$$G_{\delta t}(\mathbf{x}) = \frac{1}{(4\pi\delta t)^{n/2}} \exp(-\frac{|\mathbf{x}|^2}{4\delta t})$$

is the Gaussian kernel.

In the total energy (3), the second and third terms are surface energies defined on the solid surface Γ. They are the solid-liquid interfacial energy term on $\Sigma_{SL} = \partial D_1 \cap \Gamma$ and the solid-vapor interfacial energy term on $\Sigma_{SV} = \partial D_2 \cap \Gamma$. To approximate the two terms using the Gaussian kernel, we extend the domain Ω beyond Γ (see Figure 2). The extended domain is $\tilde{\Omega} = \Omega \cup D_3$ where D_3 is the solid region. Then, the solid surface is $\Gamma = \partial\Omega \cap \partial D_3$, the solid-liquid interface is $\Sigma_{SL} = \partial D_1 \cap \partial D_3$ and the solid-vapor interface is $\Sigma_{SV} = \partial D_2 \cap \partial D_3$. Similar to (10), the total energy $\mathcal{E}$ in (3) can be approximated by

$$\begin{aligned}&\mathcal{E}^{\delta t}(\chi_{D_1}, \chi_{D_2}) = \\ &\frac{\gamma_{LV}}{\sqrt{\delta t}} \int_{\tilde{\Omega}} \chi_{D_1} G_{\delta t} * \chi_{D_2} \mathrm{d}\mathbf{x} + \frac{\gamma_{SL}}{\sqrt{\delta t}} \int_{\tilde{\Omega}} \chi_{D_1} G_{\delta t} * \chi_{D_3} \mathrm{d}\mathbf{x} + \frac{\gamma_{SV}}{\sqrt{\delta t}} \int_{\tilde{\Omega}} \chi_{D_2} G_{\delta t} * \chi_{D_3} \mathrm{d}\mathbf{x}.\end{aligned} \tag{11}$$

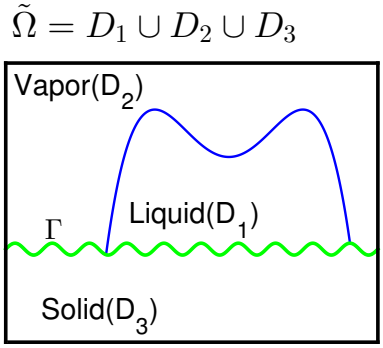

Figure 2: Extended computational domain $\tilde{\Omega} = \Omega \cup D_3$

For simplicity, we assume γ_{SL} and γ_{SV} are constants throughout this section. The analysis and the algorithms can be easily generalized to cases where they are not homogeneous. In section 5, we will apply the method to a chemically patterned surface where γ_{SL} and γ_{SV} are piecewise constant functions.

Denote $u_1 = \chi_{D_1}$ and $u_2 = \chi_{D_2}$. We define an admissible set

$$\mathcal{B} = \{(u_1, u_2) \in BV(\Omega) \mid u_i(x) = 0, 1, \text{ and } u_1(x) + u_2(x) = 1, \ a.e.\ x \in \Omega, \int_\Omega u_1 d\mathbf{x} = V_0\} \tag{12}$$

The wetting problem (3) can be approximated by

$$\min_{(u_1,u_2)\in\mathcal{B}} \mathcal{E}^{\delta t}(u_1, u_2). \tag{13}$$

This is a nonconvex minimization problem since $\mathcal{B}$ is not a convex set. The Γ-convergence of problem (13) to (3) can be proved in a similar way as in [12].

3.2. Derivation of the threshold dynamics method

We will derive the threshold dynamics method for problem (13). Notice that the problem is to minimize a concave energy functional defined on a nonconvex admissible set. We first show that it can be relaxed to a problem defined on a convex admissible set. Then we derive a threshold dynamics method for the equivalent problem. The relaxed problem is given by

$$\min_{(u_1,u_2)\in\mathcal{K}} \mathcal{E}^{\delta t}(u_1, u_2). \tag{14}$$

where $\mathcal{K}$ is the convex hull of the admissible set $\mathcal{B}$:

$$\mathcal{K} = \{(u_1, u_2) \in BV(\Omega) | 0 \le u_i \le 1, u_1(x) + u_2(x) = 1, \ a.e.\ x \in \Omega, \int_\Omega u_1 d\mathbf{x} = V_0\}. \tag{15}$$

The following lemma shows that the relaxed problem (14) is equivalent to the original problem (13). For convenience later, we prove the result for a slightly more general problem with an extra linear functional term $\mathcal{L}(u_1, u_2)$.

Lemma 3.1. *For any given $\alpha, \beta \geq 0$ and any linear functional $\mathcal{L}(u_1, u_2)$, we have*

$$\min_{(u_1,u_2)\in\mathcal{K}} (\alpha\mathcal{E}^{\delta t}(u_1, u_2) + \beta\mathcal{L}(u_1, u_2)) = \min_{(u_1,u_2)\in\mathcal{B}} (\alpha\mathcal{E}^{\delta t}(u_1, u_2) + \beta\mathcal{L}(u_1, u_2)).$$

Proof. Let $(\tilde{u}_1, \tilde{u}_2) \in \mathcal{K}$ be a minimizer of the functional

$$\alpha\mathcal{E}^{\delta t}(u_1, u_2) + \beta\mathcal{L}(u_1, u_2).$$

Since $\mathcal{B} \subset \mathcal{K}$, we have

$$\begin{aligned}\alpha\mathcal{E}^{\delta t}(\tilde{u}_1, \tilde{u}_2) + \beta\mathcal{L}(\tilde{u}_1, \tilde{u}_2) &= \min_{(u_1,u_2)\in\mathcal{K}} \alpha\mathcal{E}^{\delta t}(u_1, u_2) + \beta\mathcal{L}(u_1, u_2) \\ &\leq \min_{(u_1,u_2)\in\mathcal{B}} \alpha\mathcal{E}^{\delta t}(u_1, u_2) + \beta\mathcal{L}(u_1, u_2).\end{aligned}$$

Therefore, we need only to prove that $(\tilde{u}_1, \tilde{u}_2) \in \mathcal{B}$.

The proof is trivial when $\alpha = 0$, since the minimizer of a linear functional in a convex set must belong to the boundary of the set. When $\alpha > 0$, we prove by contradiction. If $(\tilde{u}_1, \tilde{u}_2) \notin \mathcal{B}$, there is a set $A \in \Omega$ and a constant $0 < C_0 < \frac{1}{2}$, such that $|A| > 0$ and

$$0 < C_0 < \tilde{u}_1(x), \tilde{u}_2(x) < 1 - C_0, \quad \text{for all } x \in A.$$

We divide A into two sets $A = A_1 \cup A_2$ such that $A_1 \cap A_2 = \emptyset$ and $|A_1| = |A_2| = |A|/2$. Denote $u_1^t = \tilde{u}_1 + t\chi_{A_1} - t\chi_{A_2}$ and $u_2^t = \tilde{u}_2 - t\chi_{A_1} + t\chi_{A_2}$. When $0 < t < C_0$, we have $0 < u_1^t, u_2^t < 1$ and

$$u_1^t + u_2^t = \tilde{u}_1 + \tilde{u}_2 = 1, \text{ and } \int_\Omega u_1^t \mathrm{d}\mathbf{x} = \int_\Omega \tilde{u}_1 \mathrm{d}\mathbf{x} = V_0.$$

This implies that $(u_1^t, u_2^t) \in \mathcal{K}$. Furthermore, direct computations give,

$$\begin{aligned}\frac{d^2}{dt^2}(\alpha\mathcal{E}^{\delta t}(u_1^t, u_2^t) + \beta\mathcal{L}(u_1^t, u_2^t)) &= \frac{1}{\sqrt{\delta t}} \int_{\tilde{\Omega}} \frac{d}{dt} u_1^t G_{\delta t} * \frac{d}{dt} u_2^t \mathrm{d}\mathbf{x} \\ &= \frac{1}{\sqrt{\delta t}} \int_{\tilde{\Omega}} (\chi_{A_1} - \chi_{A_2}) G_{\delta t} * (\chi_{A_2} - \chi_{A_1}) \mathrm{d}\mathbf{x} \\ &= -\frac{1}{\sqrt{\delta t}} \int_{\tilde{\Omega}} (\chi_{A_1} - \chi_{A_2}) G_{\delta t} * (\chi_{A_1} - \chi_{A_2}) \mathrm{d}\mathbf{x} \\ &< 0.\end{aligned}$$

The functional is concave on the point $(\tilde{u}_1, \tilde{u}_2)$. Thus, $(\tilde{u}_1, \tilde{u}_2)$ cannot be a minimizer of the functional. This contradicts the assumption. □

The above lemma implies that we can solve the relaxed problem (14) instead of the original one (13). In the following, we show that the problem can be solved iteratively using a thresholding method.

Suppose we solve problem (14) using an iterative method. In the k^{th} step, we have an approximated solution (u_1^k, u_2^k). The energy functional $\mathcal{E}^{\delta t}(u_1, u_2)$ can be linearized near the point (u_1^k, u_2^k) as follows:

$$\mathcal{E}^{\delta t}(u_1, u_2) \approx \mathcal{E}^{\delta t}(u_1^k, u_2^k) + \hat{\mathcal{L}}(u_1 - u_1^k, u_2 - u_2^k, u_1^k, u_2^k) + h.o.t.$$

with

$$\hat{\mathcal{L}}(u_1, u_2, u_1^k, u_2^k) = \\ \frac{1}{\sqrt{\delta t}} \left(\int_{\tilde{\Omega}} u_1 G_{\delta t} * (\gamma_{LV} u_2^k + \gamma_{SL} \chi_{D_3}) \mathrm{d}\mathbf{x} + \int_{\tilde{\Omega}} u_2 G_{\delta t} * (\gamma_{LV} u_1^k + \gamma_{SV} \chi_{D_3}) \mathrm{d}\mathbf{x} \right). \tag{16}$$

Then we minimize the linearized functional

$$\min_{(u_1, u_2) \in \mathcal{K}} \hat{\mathcal{L}}(u_1, u_2, u_1^k, u_2^k) \tag{17}$$

and set the solution to (u_1^{k+1}, u_2^{k+1}). By Lemma 3.1, the solution to (17) is in $\mathcal{B}$. In other words, u_1^{k+1} and u_2^{k+1} are characteristic functions of some proper sets D_1^{k+1} and D_2^{k+1} such that $|D_1^{k+1}| = V_0$.

The following lemma shows that the minimizing problem (17) is solved via a simple thresholding approach.

Lemma 3.2. *Denote*

$$\phi_1 = \frac{1}{\sqrt{\delta t}} G_{\delta t} * (\gamma_{LV} u_2^k + \gamma_{SL} \chi_{D_3}), \ \phi_2 = \frac{1}{\sqrt{\delta t}} G_{\delta t} * (\gamma_{LV} u_1^k + \gamma_{SV} \chi_{D_3}). \tag{18}$$

Let

$$D_1^{k+1} = \{x \in \Omega | \ \phi_1 < \phi_2 + \delta\} \tag{19}$$

for some δ such that $|D_1^{k+1}| = V_0$. Define $D_2^{k+1} = \Omega \setminus D_1^{k+1}$. Then $(u_1^{k+1}, u_2^{k+1}) = (\chi_{D_1^{k+1}}, \chi_{D_2^{k+1}})$ is a solution to (17).

Proof. By Lemma 3.1, we need only to prove

$$\hat{\mathcal{L}}(u_1^{k+1}, u_2^{k+1}, u_1^k, u_2^k) \leq \hat{\mathcal{L}}(u_1, u_2, u_1^k, u_2^k), \tag{20}$$

for all $(u_1, u_2) \in \mathcal{B}$.

For each $(u_1, u_2) \in \mathcal{B}$, we know $u_1 = \chi_{\hat{D}_1}$ and $u_2 = \chi_{\hat{D}_2}$ for some open sets $\hat{D}_1$, $\hat{D}_2$ in Ω, such that $\hat{D}_1 \cap \hat{D}_2 = \emptyset$, $\hat{D}_1 \cup \hat{D}_2 = \Omega$ and $|\hat{D}_1| = V_0$. Let $A_1 = \hat{D}_1 \setminus D_1^{k+1} = D_2^{k+1} \setminus \hat{D}_2$ and $A_2 = \hat{D}_2 \setminus D_2^{k+1} = D_1^{k+1} \setminus \hat{D}_1$. We must have $|A_1| = |A_2|$ due to the volume conservation property. Since $A_1 \subset D_2^{k+1}$, we have

$$\phi_1(x) \geq \phi_2(x) + \delta, \quad \forall x \in A_1.$$

Similarly, since $A_2 \in D_1^{k+1}$, we have

$$\phi_1(x) < \phi_2(x) + \delta, \quad \forall x \in A_2.$$

Therefore, we have

$$\begin{aligned}
&\hat{\mathcal{L}}(u_1^{k+1}, u_2^{k+1}, u_1^k, u_2^k) - \hat{\mathcal{L}}(u_1, u_2, u_1^k, u_2^k) \\
=& \int_{\tilde{\Omega}} (u_1^{k+1} - u_1)\phi_1 + (u_2^{k+1} - u_2)\phi_2 \mathrm{d}\mathbf{x} \\
=& -\int_{A_1} \phi_1 \mathrm{d}\mathbf{x} + \int_{A_2} \phi_1 \mathrm{d}\mathbf{x} - \int_{A_2} \phi_2 \mathrm{d}\mathbf{x} + \int_{A_1} \phi_2 \mathrm{d}\mathbf{x} \\
=& \int_{A_1} (\phi_2 - \phi_1)\mathrm{d}\mathbf{x} + \int_{A_2} (\phi_1 - \phi_2)\mathrm{d}\mathbf{x} \\
\leq& -\delta \int_{A_1} \mathrm{d}\mathbf{x} + \delta \int_{A_2} \mathrm{d}\mathbf{x} = 0.
\end{aligned}$$

□

We are led to the following threshold dynamics algorithm:

Algorithm I:

Step 0. *Given initial $D_1^0, D_2^0 \subset \Omega$, such that $D_1^0 \cap D_2^0 = \emptyset$, $D_1^0 \cup D_2^0 = \Omega$ and $|D_1^0| = V_0$. Set a tolerance parameter $\varepsilon > 0$.*

Step 1. *For given sets (D_1^k, D_2^k), we define two functions*

$$\phi_1 = \frac{1}{\sqrt{\delta t}} G_{\delta t} * (\gamma_{LV}\chi_{D_2^k} + \gamma_{SL}\chi_{D_3}),\ \phi_2 = \frac{1}{\sqrt{\delta t}} G_{\delta t} * (\gamma_{LV}\chi_{D_1^k} + \gamma_{SV}\chi_{D_3}). \tag{21}$$

Step 2. *Find a δ such that the set*

$$\tilde{D}_1^\delta = \{x \in \Omega | \phi_1 < \phi_2 + \delta.\} \tag{22}$$

satisfies $|\tilde{D}_1^\delta| = V_0$. Denote $D_1^{k+1} = \tilde{D}_1^\delta$ and $D_2^{k+1} = \Omega \setminus D_1^{k+1}$.

Step 3. *If $|D_1^k - D_1^{k+1}| \leq \varepsilon$, stop; otherwise, go back to Step 1.*

Remark 3.1. *The method is simple and easy to implement.*

(1) We can always extend Ω to a cubic domain $\tilde{\Omega}$, since the only constraints on the extension are $D_1 \in \tilde{\Omega}$ and $|D_1| = V_0$. For the cube domain, the convolution in (21) can be computed by fast algorithms (e.g. the FFT).

(2) To keep the volume of the liquid phase unchanged, we need to find a proper δ in Step 2. This can be done by using an iterative method (such as bisection method), as shown in [28] for mean curvature flow. In the next section, we will give a simpler and more efficient technique to determine δ.

(3) The above derivation of the thresholding method for the wetting problem can be easily generalized to a multiphase system with wetting boundary conditions, e.g. the three-phase system [29], in the same spirit of Esedoglu and Otto [12].

3.3. A simplified algorithm for the two-phase problem

For the two-phase problem, Algorithm I can be simplified as follows. Noticing that $u_1 + u_2 = 1$ in Ω, we actually have only one unknown u_1 in (14). Define

$$\mathcal{K}_1 = \{u \in BV(\Omega) | 0 \le u \le 1,\ a.e.\ x \in \Omega, \int_\Omega u \mathrm{d}\mathbf{x} = V_0\}.$$

It is easy to see that (14) can be rewritten as

$$\begin{aligned}\min_{u_1 \in \mathcal{K}_1} \tilde{\mathcal{E}}^{\delta t}(u_1) = &-\gamma_{LV} \int_{\tilde{\Omega}} u_1 G_{\delta t} * u_1 \mathrm{d}\mathbf{x} + \gamma_{LV} \int_{\tilde{\Omega}} u_1 G_\delta * \chi_\Omega \mathrm{d}\mathbf{x} \\ &+ \int_{\tilde{\Omega}} (\gamma_{SL} - \gamma_{SV}) u_1 G_{\delta t} * \chi_{D_3} \mathrm{d}\mathbf{x} + \int_{\tilde{\Omega}} \gamma_{SV} \chi_\Omega G_{\delta t} * \chi_{D_3} \mathrm{d}\mathbf{x}. \end{aligned} \tag{23}$$

Suppose we solve the problem using an iterative method. For any given u_1^k, we could linearize the functional as

$$\tilde{\mathcal{E}}^{\delta t}(u_1) = \tilde{\mathcal{E}}^{\delta t}(u_1^k) + \tilde{\mathcal{L}}(u - u_1^k, u_1^k) + h.o.t.$$

with

$$\begin{aligned}\tilde{\mathcal{L}}(u, u_1^k) = &-2\gamma_{LV} \int_{\tilde{\Omega}} u_1 G_{\delta t} * u_1^k \mathrm{d}\mathbf{x} + \gamma_{LV} \int_{\tilde{\Omega}} u_1 G_\delta * \chi_\Omega \mathrm{d}\mathbf{x} \\ &+ \int_{\tilde{\Omega}} (\gamma_{SL} - \gamma_{SV}) u_1 G_{\delta t} * \chi_{D_3} \mathrm{d}\mathbf{x} \\ =&\gamma_{LV} \int_{\tilde{\Omega}} u_1 G_{\delta t} * (u_2^k - u_1^k) \mathrm{d}\mathbf{x} + \int_{\tilde{\Omega}} (\gamma_{SL} - \gamma_{SV}) u_1 G_{\delta t} * \chi_{D_3} \mathrm{d}\mathbf{x} \\ =&\gamma_{LV} \int_{\tilde{\Omega}} u_1 G_{\delta t} * (u_2^k - u_1^k - \cos\theta_Y \chi_{D_3}) \mathrm{d}\mathbf{x}. \end{aligned} \tag{24}$$

Here we use Young's equation $\gamma_{LV} \cos\theta_Y = \gamma_{SV} - \gamma_{SL}$.

As in the previous subsection, for the linearized functional (24), we can prove the following result. The proof is similar to that for Lemma (3.2).

Lemma 3.3. *Suppose $u_1^k = \chi_{D_1^k}$ for some sets $D_1^k \subset \Omega$ and $D_2^k = \Omega \setminus D_1^k$. Denote*

$$\phi = \frac{\gamma_{LV}}{\sqrt{\delta t}} G_{\delta t} * (\chi_{D_2^k} - \chi_{D_1^k} - \cos(\theta_Y)\chi_{D_3}),$$

Let $\tilde{D}_1^\delta = \{x \in \Omega \mid \phi < \delta\}$, with some δ such that $|D_1^{k+1}| = V_0$. Then $u_1^{k+1} = \chi_{D_1^{k+1}}$ is a minimizer of $\tilde{\mathcal{L}}(u, u_1^k)$ in $\mathcal{K}_1$.

This leads to the following algorithm.

Algorithm II:

Step 0. *Given initial $D_1^0 \subset \Omega$, such that $|D_1^0| = V_0$. Set a tolerance parameter $\varepsilon > 0$.*

Step 1. *For given set D_1^k, set $D_2^k = \Omega \setminus D_1^k$, define a function*

$$\phi = \frac{\gamma_{LV}}{\sqrt{\delta t}} G_{\delta t} * (\chi_{D_2^k} - \chi_{D_1^k} - \cos(\theta_Y)\chi_{D_3}). \tag{25}$$

Step 2. *Find a $\delta \in (-1, 1)$, so that the set*

$$\tilde{D}_1^\delta = \{x \in \Omega \mid \phi < \delta.\} \tag{26}$$

satisfying $|\tilde{D}_1^\delta| = V_0$. Denote $D_1^{k+1} = \tilde{D}_1^\delta$.

Step 3. *If $|D_1^k - D_1^{k+1}| \leq \varepsilon$, stop; otherwise, go back to Step 1.*

The following proposition shows that Algorithm I and Algorithm II are equivalent.

Proposition 3.1. *For any domain $(D_1^k, D_2^k) \in \mathcal{B}$, after one iteration, Algorithm I and Algorithm II generate the same (D_1^{k+1}, D_2^{k+1}).*

Proof. We need only consider the thresholding equations (22) and (26). Direct computations give

$$\begin{aligned}
\phi_1 - \phi_2 =& \frac{1}{\sqrt{\delta t}} G_{\delta t} * (\gamma_{LV}\chi_{D_2^k} + \gamma_{SL}\chi_{D_3}) - \frac{1}{\sqrt{\delta t}} G_{\delta t} * (\gamma_{LV}\chi_{D_1^k} + \gamma_{SV}\chi_{D_3}) \\
=& \frac{1}{\sqrt{\delta t}} G_{\delta t} * \Big(\gamma_{LV}(\chi_{D_2^k} - \chi_{D_1^k}) + (\gamma_{SL} - \gamma_{SV})\chi_{D_3}\Big) \\
=& \frac{\gamma_{LV}}{\sqrt{\delta t}} G_{\delta t} * (\chi_{D_2^k} - \chi_{D_1^k} - \cos\theta_Y \chi_{D_3}) = \phi.
\end{aligned}$$

In the last equation, we used Young's equation. Therefore, the thresholding equation (22) is equivalent to the thresholding equation (26).

□

3.4. Stability analysis

In this subsection, we will show that the two algorithms above are stable, in the sense that the total energy of $\mathcal{E}^{\delta t}$ always decreases in the algorithm for any $\delta t > 0$. We have the following theorem.

Theorem 3.1. *Denote $(u_1^k, u_2^k) = (\chi_{D_1^k}, \chi_{D_2^k})$, $k = 0, 1, 2, ...$, obtained in Algorithm I (or Algorithm II). We have*

$$\mathcal{E}^{\delta t}(u_1^{k+1}, u_2^{k+1}) \leq \mathcal{E}^{\delta t}(u_1^k, u_2^k), \tag{27}$$

for all $\delta t > 0$.

Proof. By Proposition 3.1, we need only to prove the theorem for Algorithm I. By the definition of the linearization $\hat{\mathcal{L}}$ and Lemma 3.2, we know that

$$\begin{aligned}
&\mathcal{E}^{\delta t}(u_1^k, u_2^k) + \frac{\gamma_{LV}}{\sqrt{\delta t}} \int_{\tilde{\Omega}} u_1^k G_{\delta t} * u_2^k \mathrm{d}\mathbf{x} = \hat{\mathcal{L}}(u_1^k, u_2^k, u_1^k, u_2^k) \\
&\geq \mathcal{L}(u_1^{k+1}, u_2^{k+1}, u_1^k, u_2^k) = \mathcal{E}^{\delta t}(u_1^{k+1}, u_2^{k+1}) \\
&\quad + \frac{\gamma_{LV}}{\sqrt{\delta t}} \left(\int_{\tilde{\Omega}} u_1^{k+1} G_{\delta t} * u_2^k \mathrm{d}\mathbf{x} + \int_{\tilde{\Omega}} u_2^{k+1} G_{\delta t} * u_1^k \mathrm{d}\mathbf{x} - \int_{\tilde{\Omega}} u_1^{k+1} G_{\delta t} * u_2^{k+1} \mathrm{d}\mathbf{x} \right).
\end{aligned}$$

This leads to

$$\mathcal{E}^{\delta t}(u_1^k, u_2^k) \geq \mathcal{E}^{\delta t}(u_1^{k+1}, u_2^{k+1}) + I, \tag{28}$$

with

$$\begin{aligned}
I = \frac{\gamma_{LV}}{\sqrt{\delta t}} \Big(&\int_{\tilde{\Omega}} u_1^{k+1} G_{\delta t} * u_2^k \mathrm{d}\mathbf{x} + \int_{\tilde{\Omega}} u_2^{k+1} G_{\delta t} * u_1^k \mathrm{d}\mathbf{x} \\
&- \int_{\tilde{\Omega}} u_1^{k+1} G_{\delta t} * u_2^{k+1} \mathrm{d}\mathbf{x} - \int_{\tilde{\Omega}} u_1^k G_{\delta t} * u_2^k \mathrm{d}\mathbf{x} \Big) \\
= -\frac{\gamma_{LV}}{\sqrt{\delta t}} &\int_{\tilde{\Omega}} (u_1^{k+1} - u_1^k) G_{\delta t} * (u_2^{k+1} - u_2^k) \mathrm{d}\mathbf{x}.
\end{aligned}$$

By the fact that $u_1^k + u_2^k = u_1^{k+1} + u_2^{k+1}$, we have

$$I = \frac{\gamma_{LV}}{\sqrt{\delta t}} \int_{\tilde{\Omega}} (u_1^{k+1} - u_1^k) G_{\delta t} * (u_1^{k+1} - u_1^k) \mathrm{d}\mathbf{x} \geq 0.$$

This inequality together with (28) implies (27). □

4. Numerical implementation and accuracy check

In this section, we will introduce several techniques used to implement the algorithm efficiently.

4.1. Calculation of convolution

In Algorithm I, we need to calculate the two convolutions $G_{\delta t} * (\gamma_{LV} \chi_{D_2^k} + \gamma_{SL} \chi_{D_3})$ and $G_{\delta t} * (\gamma_{LV} \chi_{D_1^k} + \gamma_{SV} \chi_{D_3})$ in an extended domain $\tilde{\Omega}$ which we can always choose to be a rectangular domain. We can use FFT to efficiently calculate the convolutions when the functions are periodic. In our simulation, the characteristic functions (e.g. $\gamma_{LV} \chi_{D_2^k} + \gamma_{SL} \chi_{D_3}$) are not periodic. To calculate convolutions for non-periodic functions, we can further extend the domain by reflection so that the functions are periodic in the extended domain. However, the heat kernel $G_{\delta t}$ decays exponentially and is negligible when $|x| > 10\sqrt{\delta t}$. When we calculate the convolution, each target point will only be affected by a few neighboring points. Hence, if we apply the FFT without extending the computational domain, we will only have some error near the boundary of the computational domain (See Figure 3). When the dynamic interface is far away from the boundary of the computational domain, the solutions calculated with or without the domain extension are the same, after the thresholding step. Therefore, in our calculation, we always directly apply the FFT without extending the computational domain.

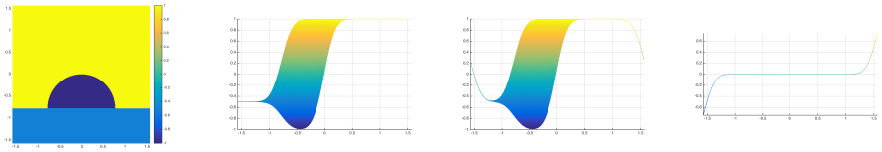

Figure 3: From left to right: 1. The initial condition defined by the characteristic function of the domains. 2. The X-Z plane of the convolution between the heat kernel and the initial condition calculated by extending the domain by reflection (i.e. extending $[-\frac{\pi}{2}, \frac{\pi}{2}] \times [-\frac{\pi}{2}, \frac{\pi}{2}]$ to $[-\frac{\pi}{2}, \frac{3\pi}{2}] \times [-\frac{\pi}{2}, \frac{3\pi}{2}]$). 3. The X-Z plane of the convolution between the heat kernel and the initial condition calculated without extending the domain. 4. The difference between the second figure and the third figure.

4.2. A quicksort algorithm for volume preservation

In Step 2 of Algorithm I, we need to enforce volume preservation. This is achieved by shifting the thresholding level by δ as in (22). The usual way to find δ is by some iteration method (e.g. bisection method, Newton method, fixed point iteration, see [28]). However, these iterative methods may be sensitive to the initial guess. In this section, we will introduce a direct and more efficient algorithm to find a proper δ. If we consider a uniform mesh (in two dimensions) and denote the mesh size by dx, the volume of a domain can be approximated by $V_0 \approx M \times dx^2$ (with first-order accuracy). To maintain the same volume after thresholding, what we need to do in Step 2 is to find a threshold δ such that there are M grid values of $\phi_1 - \phi_2 = g$ which are less than δ. Since we have the values of $\phi_1 - \phi_2$ at each grid point, we can use the quicksort algorithm (available in Matlab) [16] to sort the values in ascending order into a list $\mathcal{S} = \{g_1, g_2, ..., g_M, g_{M+1}, ...\}$. We then take the average of the M^{th} value and $(M+1)^{th}$ value in the ordered list $\mathcal{S}$, i.e. $\delta = \frac{g_M + g_{M+1}}{2}$ to be the threshold value δ. A simple example to demonstrate this fast scheme is shown in Figure 4. The scheme is summarized as follows:

A quicksort scheme for volume conservation

Step 0. *Set V_0 as the volume to be preserved and M as the integer part of V_0/dx^2.*

Step 1. *Use a quicksort algorithm to sort $g = \phi_1 - \phi_2$, which is defined in Step 2 in Algorithm 2, in ascending order into a list $\mathcal{S} = \{g_1, g_2, ..., g_M, g_{M+1}, ...\}$.*

Step 2. *Set $\delta = \frac{g_M + g_{M+1}}{2}$.*

In summary, the computational complexity involved in finding δ is $O(N \log(N))$ when the quicksort algorithm is used. It is straightforward to see that this scheme will give the same δ as the iterative scheme proposed by Ruuth [28] (with first order accuracy). However, our scheme costs much less computationally.

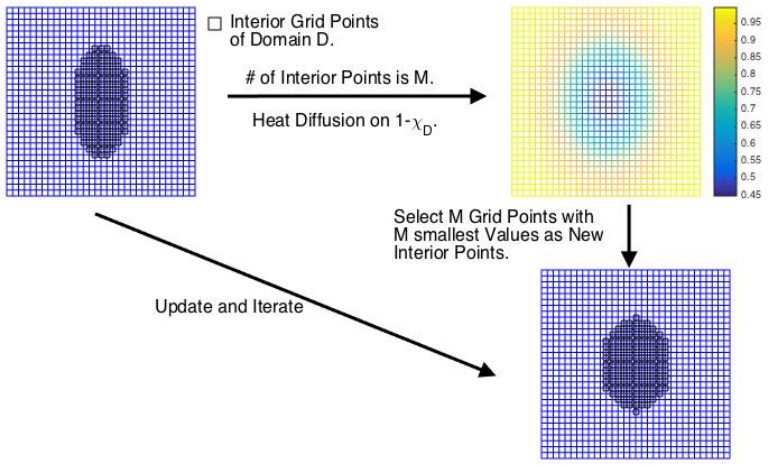

Figure 4: An example to demonstrate our new scheme for volume preservation. Initially, there are M interior points. After convolution, we select M grid points with the M lowest values as the new interior points.

Table 1: Accuracy check of Algorithm I for the two circle motion

δt	Volume Error	Convergence Rate	L^∞ Error	Convergence Rate
0.002	-0.0033	–	0.0074	–
0.001	-0.0015	1.15	0.0023	2.20
0.0005	-0.00079	1.14	0.0011	1.08
0.00025	-0.00035	1.03	0.00061	0.81

4.3. Accuracy check of Algorithm I

In this subsection, we will check the accuracy of Algorithm I. We first consider an example of motion of two circles. One circle is centered at $(0.35, 0.35)$ with radius 0.2 and the other is centered at $(0.7, 0.7)$ with radius 0.15 (see in Figure 5). The volume-preserving mean curvature flow is governed by the interface motion law $v_n = \kappa - \kappa_a$, where v_n represents the normal velocity of the interface, κ is the curvature and κ_a is the average curvature of the interface. By this motion, the larger circle will grow in volume while the smaller circle will shrink gradually. The exact solution can be calculated and the area enclosed by the smaller circle after a time $t = 0.02$ is given by 0.0445079 [28]. Using Algorithm I, we compute numerically the motion of the two circles and compare the results with the exact solution. Table 1 shows the volume error as well as L^∞ error compared with the exact solution at $t = 0.02$ for different $\delta t = (0.002, 0.001, 0.0005, 0.00025)$ with the same spatial resolution (4096×4096). The results indicate the first-order accuracy of our scheme.

We next consider the motion of two semi-circles on the solid surface. One is centered at $(0.3, 0.25)$ with

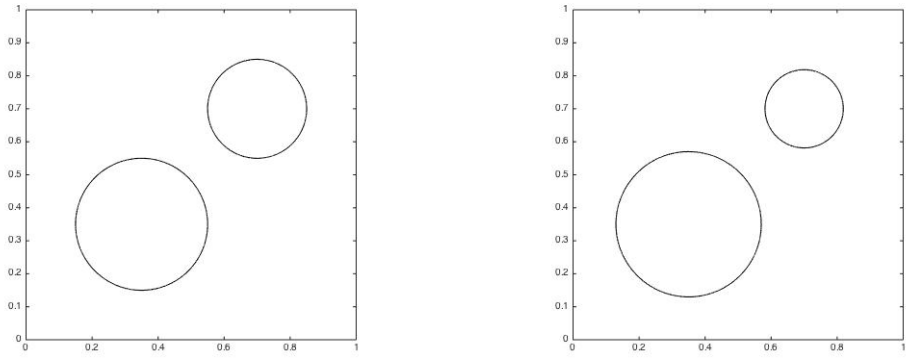

Figure 5: The two circles at $t = 0$ (left) and $t = 0.02$(right).

radius 0.2 and the other one is centered at $(0.8, 0.25)$ with radius 0.15 (See Figure 6). In this problem, we set Young's angle to $\pi/2$. Then the wetting boundary condition in (5) will reduce to a homogeneous Neumann boundary condition. One can obtain the same motion as that of two full circles by symmetric reflection. Therefore, the exact solution can also be calculated and the area enclosed by the smaller semi-circle after a time $t = 0.02$ is 0.022254 (half of the volume of the smaller circle in the previous example). Again, using Algorithm I, we compute numerically the motion of the two circles and compare the results with the exact solution. Table 2 shows the volume error as well as L^∞ error compared with the exact solution at $t = 0.02$ for different $\delta t = (0.002, 0.001, 0.0005, 0.00025)$ with the same spatial resolution (4096×4096). The results show first-order accuracy for volume preservation but a half-order convergence for L^∞ norm. This is typical for multi-phase problems with a junction.

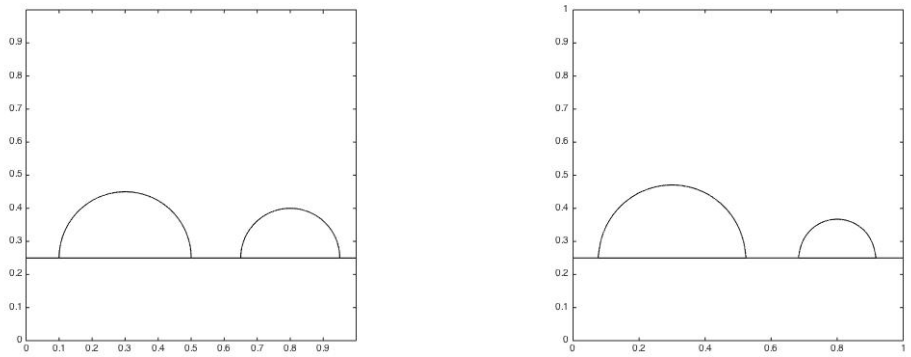

Figure 6: The two semi-circles at $t = 0$ (left) and $t = 0.02$(right).

Finally, we consider the case of drop spreading on a solid surface with a general static contact angle. The initial drop is a semi-circle centered at $(0, -\frac{\pi}{4})$ with a radius $\frac{\pi}{4}$ (see Figure 7). We set three surface tensions

Table 2: Accuracy check of Algorithm I for the motion of two semi-circles on solid boundary.

δt	Volume Error	Convergence Rate	L^∞ Error	Convergence Rate
0.002	-0.0071	–	0.030	–
0.001	-0.0033	1.17	0.011	1.78
0.0005	-0.0016	1.03	0.0057	0.88
0.00025	-0.00092	0.75	0.0035	0.62

Table 3: Accuracy check w.r.t the time step δt for the drop spreading problem.

δt	L^1 Error	Convergence Rate	L^∞ Error	Convergence Rate
0.04	0.0676	–	0.0928	–
0.02	0.0347	0.95	0.0621	0.49
0.01	0.0170	1.04	0.0383	0.62
0.005	0.0079	1.14	0.0215	0.79

to $\gamma_{LV} = 1, \gamma_{LS} = 1$ and $\gamma_{SV} = 1 + \sqrt{3}/2$ which gives Young's angle $\frac{\pi}{3}$. Thus the drop will spread and its contact angle decreases gradually to Young's angle. Since we do not know the exact solution in this case, the reference solution of the liquid-vapor interface after time $t = 0.2$ is numerically computed by choosing sufficiently small $\delta t = 0.00125$ and $dx = \frac{\pi}{4096}$. We then compare the numerical solution with the reference solution for different $\delta t = 0.04, 0.02, 0.01, 0.005$ but with the same $dx = \frac{\pi}{4096}$. The results are shown in Table 3, which suggests a first-order convergence rate in L^1 error and a half-order convergence rate in L^∞ error.

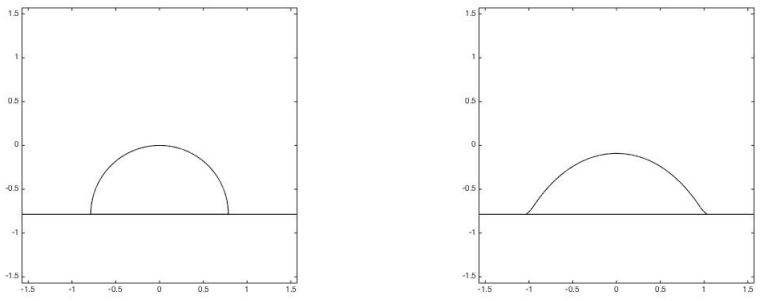

Figure 7: The shape of a drop at $t = 0$ (left) and $t = 0.2$(right).

4.4. A time refinement scheme for contact point motion

For any given space mesh, the only parameter in Algorithm I is the time step δt. According to Merriman, Bence and Osher [22], the choice of δt should meet two requirements. The first one is that δt should be small enough so that the approximation of the energy is reasonably accurate. The second is that δt should also be large enough so that the boundary curve moves at least one grid cell on the spatial grid (otherwise the interface would not move after the thresholding step), that is, $\delta t \gg \frac{\delta x}{\kappa}$ where κ is the average curvature and δx is the space mesh size. Since we have volume conservation, the interface will eventually become circular with a constant curvature. Therefore, for a given space mesh size δx, there is a δt threshold below which the interface will not move. Therefore time step refinement beyond this threshold will not improve the accuracy of the interface location. However, when the interface intersects the solid boundary, the motion of the contact point follows different dynamics and is controlled by the Young stress $f = \gamma_{LV}(\cos\theta - \cos\theta_Y)$. This may lead to a different time scale (and a different time step constraint). Numerical results show that time step refinement improves the accuracy near the contact point. Hence, we propose a time refinement scheme to minimize the interfacial energy. The idea is to first use a proper (large enough) time step δt so that the evolution of the interface reaches equilibrium. We then improve the contact point accuracy by repeatedly halving the time step δt until the difference between the solutions of succeeding steps is within a tolerance ε_1.

Modified Algorithm I

Step 0. *Given initial $D_1^0, D_2^0 \subset \Omega$, such that $D_1^0 \cap D_2^0 = \emptyset$, $D_1^0 \cup D_2^0 = \Omega$ and $|D_1^0| = V_0$. Set $D_1^* = D_1^0$. Set a tolerance parameter $\varepsilon > 0$.*

Step 1. *For given set (D_1^k, D_2^k), we define two functions*

$$\phi_1 = \frac{1}{\sqrt{\delta t}} G_{\delta t} * (\gamma_{LV}\chi_{D_2^k} + \gamma_{SL}\chi_{D_3}),\ \phi_2 = \frac{1}{\sqrt{\delta t}} G_{\delta t} * (\gamma_{LV}\chi_{D_1^k} + \gamma_{SV}\chi_{D_3}). \tag{29}$$

Step 2. *Find a constant δ to ensure volume preservation using the quick-sort algorithm in section 4.2, so that the set*

$$\tilde{D}_1^\delta = \{x \in \Omega | \phi_1 < \phi_2 + \delta.\} \tag{30}$$

satisfying $|\tilde{D}_1^\delta| \approx V_0$. Denote $D_1^{k+1} = \tilde{D}_1^\delta$, $D_2^{k+1} = \Omega \setminus D_1^{k+1}$.

Step 3. *IF $|D_1^k - D_1^{k+1}| \le \varepsilon$,*

if $|D_1^* - D_1^{k+1}| \ge \varepsilon$,set $\delta t = \frac{\delta t}{2}$, $D_1^* = D_1^{k+1}$, and go back to step 1.

else, set $D_1^* = D_1^{k+1}$ and stop.

endif

ELSE, go back to step 1.

ENDIF

Table 4: Accuracy Check in L^1 norm

Grid points	L^1 error	Convergence rate	L^1 error with time refinement	Convergence rate
128× 128	0.1473	-	0.0515	–
256× 256	0.0482	2.06	0.0271	0.90
512× 512	0.0200	1.41	0.0109	1.49
1024 × 1024	0.0116	0.72	0.0054	1.02

4.5. Accuracy check of the Modified Algorithm I

To check the accuracy of the Modified Algorithm I described in Section 4.4, we consider a two-dimensional drop spreading on a solid surface. The equilibrium state is a circular arc with Young's angle when the minimum of the total interfacial energy is reached. In our experiment, the initial liquid phase is given by a semi-circle centered at $(0, -\frac{\pi}{4})$ with radius $\frac{\pi}{4}$. So the volume of the drop is $\frac{\pi^3}{32}$. We set three surface tensions as $\gamma_{LV} = 1, \gamma_{LS} = 1$ and $\gamma_{SV} = 1 + \sqrt{3}/2$, which gives Young's angle $\frac{\pi}{3}$. In this case, the exact equilibrium state can be computed explicitly.

In Figure 8, Figure 9 and Figure 10, we show the errors of solutions (characteristic functions) computed by both Algorithm I and the Modified Algorithm I, compared with the exact solution (the characteristic function of the exact equilibrium state) which shows the location error of the interface. It is obvious that the errors near contact points are much larger than those at other places of the interfaces. However, after time step refinement, the Modified Algorithm 1 gives much improved results. Figure 11 compares well the numerical solution and exact solution at the equilibrium.

We then check the accuracy of the algorithms via calculating the convergence rate of the L^1 error and L^∞ error with respect to the mesh refinement. Table 4 shows the L^1 errors of both schemes. Again the Modified Algorithm I gives much better results. The results also show that the convergence rate for L^1 error of our algorithm is of first order. Table 5 shows the L^∞ errors of both schemes. Again the Modified Algorithm I gives superior results. The example shows that the time refinement scheme improves the accuracy dramatically. But this does not necessarily mean that the convergence order is also improved, especially for the L^1 error.

5. A drop spreading on a chemically pattern solid surface

We first study the hysteresis behavior of a drop spreading on a chemically patterned surface. We consider the quasi-static spreading of a drop. To simulate the hysteresis process. we need to increase or decrease the volume of the drop gradually. In each step, we need to compute the equilibrium state of the drop after liquid

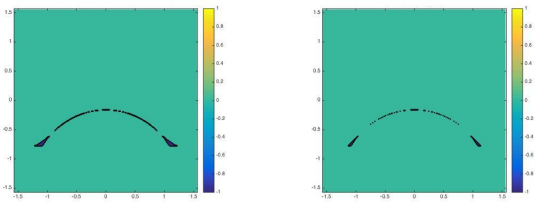

Figure 8: Left: 256×256 grid points, $\delta t = 2dx$ without refinement in time. Right: 256×256 grid points, $\delta t = 2dx$ initially with refinement in time, $\epsilon = 1.0e^{-10}$

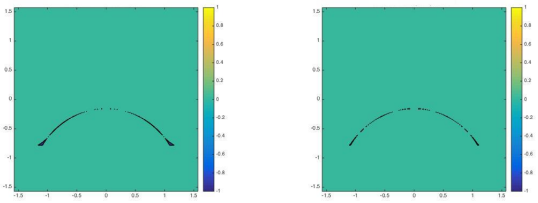

Figure 9: Left: 512×512 grid points, $\delta t = 2dx$ without refinement in time. Right: 512×512 grid points, $\delta t = 2dx$ initially with refinement in time, $\epsilon = 1.0e^{-10}$

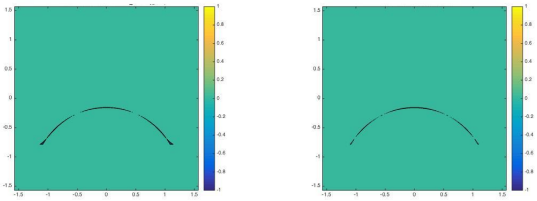

Figure 10: Left: 1024×1024 grid points, $\delta t = 2dx$ without refinement in time. Right: 1024×1024 grid points, $\delta t = 2dx$ initially with refinement in time, $\epsilon = 1.0e^{-10}$

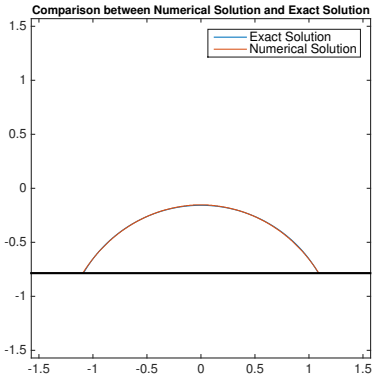

Figure 11: Comparison of the numerical solution at equilibrium to the exact solution. Red line represents the exact solution while the blue line represents the numerical solution (computed with 1024×1024 grid points).

Table 5: Accuracy Check in L^∞ norm

Grid points	L^∞ error	Convergence rate	L^∞ error with time refinement	Convergence rate
128× 128	0.1473	-	0.0982	–
256× 256	0.0831	0.77	0.0585	0.68
512× 512	0.0552	0.51	0.0307	0.91
1024 × 1024	0.0333	0.66	0.0149	1.1

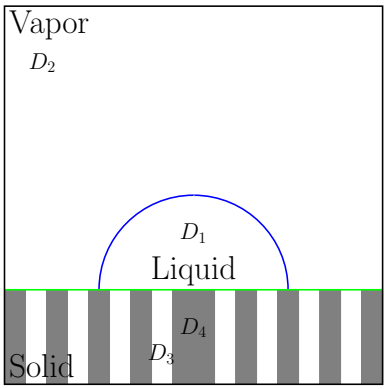

Figure 12: A sketch of a drop spreading on a chemically patterned solid surface. Here D_3 (white region) and D_4 (shaded region) represent materials $\mathcal{A}$ and $\mathcal{B}$ respectively.

is added or extracted, which is very computationally demanding. We show that our threshold dynamics method can simulate the process efficiently.

We assume that the surface is periodically patterned in the interval $(-\pi/2, \pi/2)$ and the interval is divided into $2k+1$ periods with an equal partition of two materials $\mathcal{A}, \mathcal{B}$ away from the center. The center part is occupied by the material $\mathcal{B}$ (See Figure 12). Assume $\theta_{\mathcal{A}}$, $\theta_{\mathcal{B}}$ are Young's angles for materials $\mathcal{A}$ and $\mathcal{B}$ respectively. r is the initial radius of a semi-circle on the surface and ΔV is the volume we add to the drop each time. The procedure for explicitly calculating the change in contact angle and position of contact points with respect to the volume for simple two-phase systems on a chemically patterned surface is given in [33].

To implement the Modified Algorithem I, we need to divide our solid region into two parts D_3 and D_4 representing material $\mathcal{A}$ and material $\mathcal{B}$ with different surface tensions, respectively (as shown in Figure 12), and modify the original $\gamma_{SL}\chi_{D_3}$ and $\gamma_{SV}\chi_{D_3}$ to $\gamma_{S_1L}\chi_{D_3}+\gamma_{S_2L}\chi_{D_4}$ and $\gamma_{S_1V}\chi_{D_3}+\gamma_{S_2V}\chi_{D_4}$. As the volume of the drop increases quasi-statically, we use the Modified Algorithem I to calculate the equilibrium state for each fixed volume.

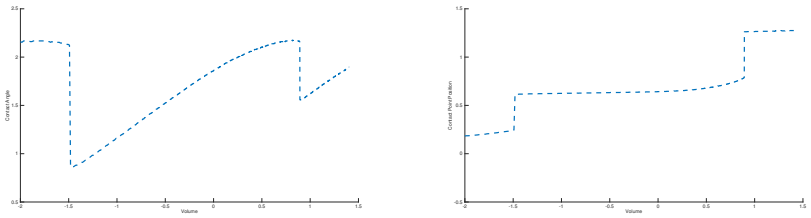

Figure 13: The stick-slip motion of a drop with k=2 when the volume is increasing. $\theta_{\mathcal{A}} = \frac{\pi}{5}$, $\theta_{\mathcal{B}} = \frac{7\pi}{10}$.

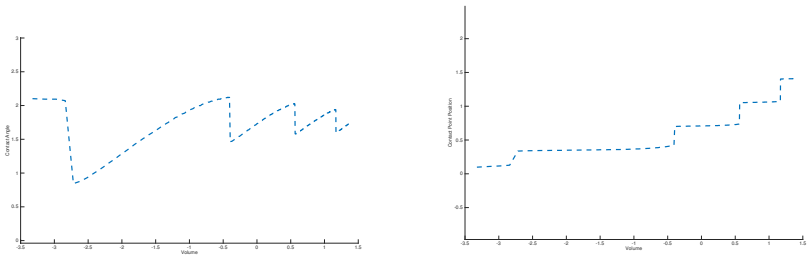

Figure 14: The stick-slip motion of a drop with k=4 when the volume is increasing. $\theta_{\mathcal{A}} = \frac{\pi}{5}$, $\theta_{\mathcal{B}} = \frac{7\pi}{10}$.

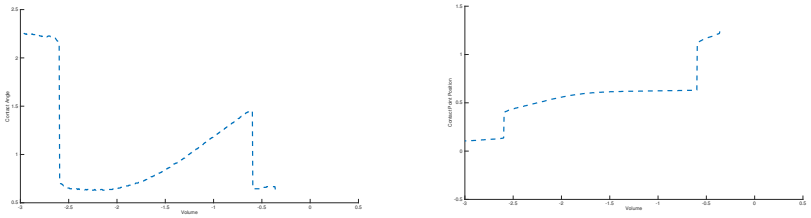

Figure 15: The stick-slip motion of a drop with k=2 when the volume is decreasing. $\theta_{\mathcal{A}} = \frac{\pi}{5}$, $\theta_{\mathcal{B}} = \frac{7\pi}{10}$.

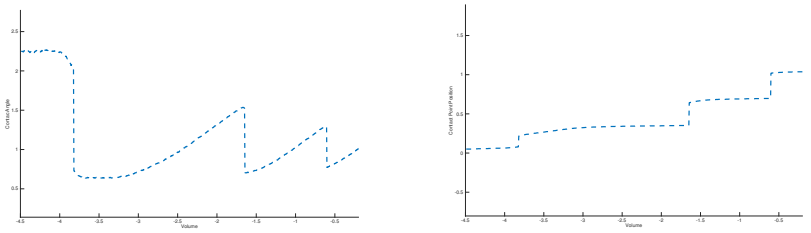

Figure 16: The stick-slip motion of a drop with k=4 when the volume is decreasing. $\theta_{\mathcal{A}} = \frac{\pi}{5}$, $\theta_{\mathcal{B}} = \frac{7\pi}{10}$.

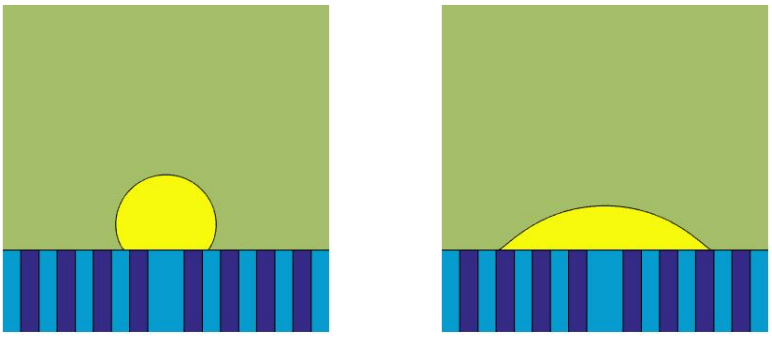

Figure 17: Left: A quasi-static drop in the process of growing in volume on a chemically patterned surface when the initial volume is 0.5883. Right: A quasi-static drop in the process of shrinking in volume on a chemically patterned surface when the initial volume is 0.5883. Young's angle in the light blue part is $\mathcal{B}$ while that in the dark blue part is $\mathcal{A}$. Here k=4.

We take $\theta_{\mathcal{A}} = \frac{\pi}{5}$, $\theta_{\mathcal{B}} = \frac{7\pi}{10}$. For the advancing drop, we plot the contact angle and position of contact point as functions of increasing volume in Figure 13 for $k = 2$ and in Figure 14 for $k = 4$. The contact point goes through the stick-slip motion, and the contact angle oscillates near the advancing angle $\theta_{\mathcal{B}}$ for larger k.

For the receding drop, we plot the contact angle and location of the contact point as functions of increasing volume in Figure 15 for $k = 2$ and in Figure 16 for $k = 4$. Again, the contact point goes through the stick-slip motion, and the contact angle oscillates near the receding angle $\theta_{\mathcal{A}}$ for larger k.

In Figure 17, we show two quasi-static drops. One is in the process of increasing in volume (advancing) and the other is in the process of decreasing in volume (receding). We see that the two states have very different contact angles although the volume is the same. This clearly shows that the contact angle hysteresis as the shape of a drop on a chemically patterned surface depends on its history.

6. A drop spreading on a rough solid surface

In this section, we will simulate the contact angle hysteresis on a geometrically rough surface. In our experiments, the computational domain is $[-\frac{\pi}{2}, \frac{\pi}{2}] \times [-\frac{\pi}{2}, \frac{\pi}{2}]$, and we take the solid surface of shape given by a sawtooth function

$$y = -\frac{\pi}{4} + \tan(\alpha)\frac{\pi}{4k+2}|s((2k+1)x - \pi)|$$

where $s(x)$ is a sawtooth periodic function with period 2π defined as

$$s(x) = \begin{cases} \frac{2}{\pi}(x+\pi) - 1 & -\pi \le x \le 0; \\ -\frac{2}{\pi}x + 1 & 0 \le x \le \pi. \end{cases}$$

For a rough surface, it is more meaningful to see how the effective contact angle behaves when the volume of the drop is increased or decreased [6]. The effective contact angle is defined as the angle between the contact

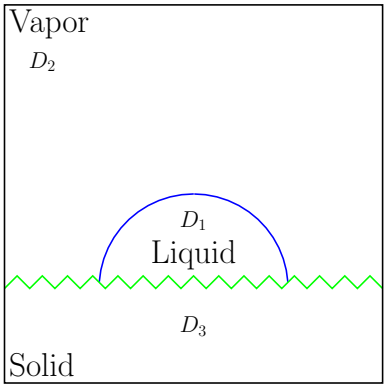

Figure 18: Left: A sketch of a drop spreading on a rough solid surface. The solid surface is given by a sawtooth profile.

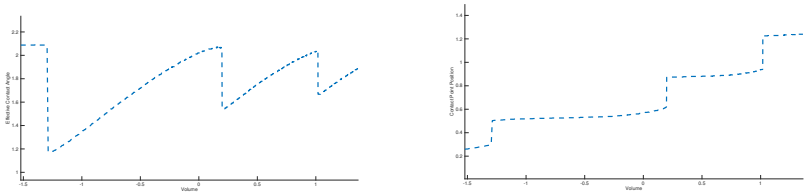

Figure 19: The stick-slip motion of a drop on a rough surface when the volume is increasing. $\theta = \frac{\pi}{2}, k = 4, \alpha = \frac{\pi}{6}$.

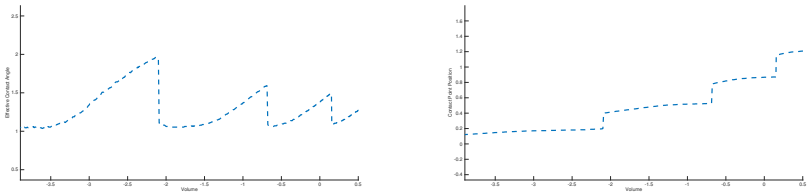

Figure 20: The stick-slip motion of a drop on a rough surface when the volume is decreasing. $\theta = \frac{\pi}{2}, k = 4, \alpha = \frac{\pi}{6}$.

Figure 21: Left: A quasi-static drop in the process of expanding in volume on a sawtooth rough surface when the volume is 1.178. Right: A quasi-static drop in the process of reducing in volume on a sawtooth rough surface when the volume is 1.178. $\theta = \frac{\pi}{2}, k = 4, \alpha = \frac{\pi}{6}$.

line and the horizontal surface (See Figure 18). Figure 19 and Figure 20 show the bahavior of the contact angle and the x-coordinate of the contact point for the case when $k = 4, \alpha = \frac{\pi}{6}$. Young's angle of the solid surface is $\theta_Y = \frac{\pi}{2}$. We can see obvious stick-slip motion when we increase or decrease the volume of the drop. Furthermore, the advancing contact angle is almost $\frac{2\pi}{3}$ and the receding contact angle is approximately $\frac{\pi}{3}$.

In Figure 21, again, we show two quasi-static drops. One is in the process of expanding in volume (advancing) and the other is in the process of reducing in volume (receding). Similar to the chemically patterned surface case, the two states have very different apparent contact angles corresponding to the contact angle hysteresis on rough surfaces.

7. Conclusion

We develop an efficient threshold dynamics method for wetting on rough surfaces. The method is based on minimization of the weighted surface area functional over an extended domain that includes the solid phase. The method is simple, stable with the complexity $O(N \log N)$ per time step and is not sensitive to the inhomogeneity or roughness of the solid boundary. The efficiency of the method can be further improved with adaptive mesh techniques with more mesh points near the interface and contact line.

Acknowledgments

This publication was based on work supported in part by the Hong Kong RGC-GRF grants 605513 and 16302715 and the RGC-CRF grant C6004-14G. XM Xu is supported in part by NSFC 11571354. We would also like to thank the anonymous referees for their valuable comments and suggestions to help us to improve the paper.

Reference

References

[1] G. Alberti and G. Bellettini. A non-local anisotropic model for phase transitions: asymptotic behaviour of rescaled energies. *Euro. J. Appl. Math.*, 9(03):261–284, 1998.

[2] G. Alberti and A. DeSimone. Wetting of rough surfaces: A homogenization approach. *Proc. R. Soc. A*, 451:79–97, 2005.

[3] G. Barles and C. Georgelin. A simple proof of convergence for an approximation scheme for computing motions by mean curvature. *SIAM J. Numer. Anal.*, 32(2):484–500, 1995.

[4] A. L. Bertozzi, S. Esedoglu, and A. Gillette. Inpainting of binary images using the cahn-hilliard equation. *IEEE Transactions on image processing*, 16(1):285–291, 2007.

[5] A. Chambolle and M. Novaga. Convergence of an algorithm for the anisotropic and crystalline mean curvature flow. *SIAM J. Math. Anal.*, 37(6):1978–1987, 2006.

[6] X. Chen, X.-P. Wang, and X. Xu. Effective contact angle for rough boundary. *Physica D: Nonlinear Phenomena*, 242(1):54–64, 2013.

[7] X. Chen, X.-P. Wang, and X. Xu. Analysis of the cahn-hilliard equation with relaxation boundary condition modelling contact angle. *Arch. Rational Mech. Anal.*, 213:1–24, 2014.

[8] P. de Gennes, F. Brochard-Wyart, and D. Quere. *Capillarity and Wetting Phenomena*. Springer Berlin, 2003.

[9] K. Deckelnick, G. Dziuk, and C. M. Elliott. Computation of geometric partial differential equations and mean curvature flow. *Acta numerica*, 14:139–232, 2005.

[10] C. M. Elliott and V. Styles. Computations of bidirectional grain boundary dynamics in thin metallic films. *Journal of Computational Physics*, 187(2):524–543, 2003.

[11] H. Y. Erbil. The debate on the dependence of apparent contact angles on drop contact area or three-phase contact line: a review. *Surface Science Reports*, 69(4):325–365, 2014.

[12] S. Esedoglu and F. Otto. Threshold dynamics for networks with arbitrary surface tensions. *Comm. Pure Appl. Math.*, 2015.

[13] S. Esedoglu, S. Ruuth, and R. Tsai. Threshold dynamics for high order geometric motions. *Interfaces and Free Boundaries*, 10(3):263–282, 2008.

[14] L. C. Evans. Convergence of an algorithm for mean curvature motion. *Indiana Math. J.*, 42(2):533–557, 1993.

[15] C. W. Extrand. Model for contact angles and hysteresis on rough and ultraphobic surfaces. *Langmuir*, 18:7991–7999, 2002.

[16] C. A. Hoare. Quicksort. *The Computer Journal*, 5(1):10–16, 1962.

[17] K. Ishii. Optimal rate of convergence of the bence–merriman–osher algorithm for motion by mean curvature. *SIAM J. Math. Anal.*, 37(3):841–866, 2005.

[18] C. Kublik, S. Esedoglu, and J. Fessler. Algorithms for area preserving flows. *SIAM J. Sci. Comput.*, 33:2382–2401, 2011.

[19] T. Laux and F. Otto. Convergence of the thresholding scheme for multi-phase mean-curvature flow. *arXiv:1602.05857.*, 2016.

[20] T. Laux and D. Swartz. Convergence of thresholding schemes incorporating bulk effects. *arXiv:1601.02467.*, 2016.

[21] S. Leung and H. Zhao. A grid based particle method for moving interface problems. *Journal of Computational Physics*, 228(8):2993–3024, 2009.

[22] B. Merriman, J. K. Bence, and S. Osher. *Diffusion generated motion by mean curvature*. Department of Mathematics, University of California, Los Angeles, 1992.

[23] B. Merriman, J. K. Bence, and S. J. Osher. Motion of multiple junctions: A level set approach. *J. Comput. Phy.*, 112(2):334–363, 1994.

[24] M. Miranda, D. Pallara, F. Paronetto, and M. Preunkert. Short-time heat flow and functions of bounded variation in r^n. In *Annales-Faculte des Sciences Toulouse Mathematiques*, volume 16, page 125. Université Paul Sabatier, 2007.

[25] D. Quere. Wetting and roughness. *Annu. Rev. Mater. Res.*, 38:71–99, 2008.

[26] S. J. Ruuth. A diffusion-generated approach to multiphase motion. *J. Comput. Phy.*, 145(1):166–192, 1998.

[27] S. J. Ruuth. Efficient algorithms for diffusion-generated motion by mean curvature. *J. Comput. Phy.*, 144(2):603–625, 1998.

[28] S. J. Ruuth and B. T. Wetton. A simple scheme for volume-preserving motion by mean curvature. *J. Sci. Comput.*, 19(1-3):373–384, 2003.

[29] Y. Shi and X.-P. Wang. Modeling and simulation of dynamics of three-component flows on solid surface. *Japan Journal of Industrial and Applied Mathematics*, 31(3):611–631, 2014.

[30] K. Svadlenka, E. Ginder, and S. Omata. A variational method for multiphase volume-preserving interface motions. *Journal of Computational and Applied Mathematics*, 257:157 – 179, 2014.

[31] G. Whyman, E. Bormashenko, and T. Stein. The rigorous derivative of young, cassie-baxter and wenzel equations and the analysis of the contact angle hysteresis phenomenon. *Chem. Phy. Letters*, 450:355–359, 2008.

[32] D. E. Womble. A front-tracking method for multiphase free boundary problems. *SIAM journal on numerical analysis*, 26(2):380–396, 1989.

[33] X. Xu and X. P. Wang. Analysis of wetting and contact angle hysteresis on chemically patterned surfaces. *SIAM J. Appl. Math.*, 71:1753–1779, 2011.

[34] X. Xu and X. P. Wang. The modified cassie's equation and contact angle hysteresis. *Colloid Polym. Sci.*, 291:299–306, 2013.

[35] T. Young. An essay on the cohesion of fluids. *Philos. Trans. R. Soc. London*, 95:65–87, 1805.

[36] H.-K. Zhao, T. Chan, B. Merriman, and S. Osher. A variational level set approach to multiphase motion. *J. Comput. Phy.*, 127(1):179–195, 1996.